Modeling of two-hot-arm horizontal thermal actuator

Modeling of two-hot-arm horizontal thermal actuator

Dong Yan, Amir Khajepour and Raafat Mansour

University of Waterloo, Waterloo, Ontario, Canada N2L 3G1

E-mail: akhajepour@uwaterloo.ca

Abstract

Electrothermal actuators have a very promising future in MEMS applications since they can generate large deflection and force with low actuating voltages and small device areas. In this study, a lumped model of a two-hot-arm horizontal thermal actuator is presented. In order to prove the accuracy of the lumped model, finite element analysis (FEA) and experimental results are provided. The two-hot-arm thermal actuator has been fabricated using the MUMPs process. Both the experimental and FEA results are in good agreement with the results of lumped modeling.

(Some figures in this article are in colour only in the electronic version)

1. Introduction

The greatest promise of microelectromechanical systems (MEMS) lies in the ability to integrate a whole system into a single chip. Besides using integrate circuits (IC) as control units, MEMS also require IC compatible and cost effective actuating units with characteristics such as large deflection and force. Several different actuators including electrostatic [1, 2], magnetic [3, 4] and electrothermal actuators [5, 6] have been well documented. Among these microactuators, electrothermal actuators are very attractive not only because they can generate larger deflection and force [7], but also because their fabrication process is compatible with general IC fabrication processes [6]. Since Guckel *et al* [5] proposed a new flexure thermal actuator in 1992, thermal actuators have been widely employed in MEMS applications [6, 8]. Based on the traditional horizontal thermal actuator with one hot arm, Burns *et al* [9] designed a new thermal actuator with two hot arms, with larger deflection and force compared to the traditional thermal actuator. Deflection of a thermal actuator strongly depends on its geometric structure and material properties. Modeling of the one-hot-arm thermal actuator has been extensively elaborated in [10–13].

In this paper, the lumped modeling of the two-hot-arm horizontal thermal actuator is presented to have a better insight into the actuator operation. The lumped model allows designers to predict the actuator performance before its fabrication. For the modeling, the electrothermal analysis is proceeded first, followed by thermal-mechanical analysis. Finite element analysis is performed to evaluate the lumped model. Fabrication and experimental studies of the thermal actuator are documented and the test results are presented. The comparisons show that the lumped model predicts the experimental results with significant accuracy and can be used as a simple and fast design tool in two-hot-arm actuators. In the end, some phenomena found during the tests are discussed and conclusion are drawn.

2. Lumped modeling analysis

A schematic of the traditional horizontal thermal actuator is shown in figure 1(*a*). It deflects because of asymmetric heating of the cold and hot arms. Since the cold and hot arms are made of the same material, the thinner hot arm has a relatively larger electrical resistance than the cold arm. When current passes through the cold and hot arms, the hot arm is resistively heated to a higher temperature. Hence, the hot arm expands in length more than the cold arm. The difference of the expansion between the cold and hot arms causes the actuator to rotate about the flexure.
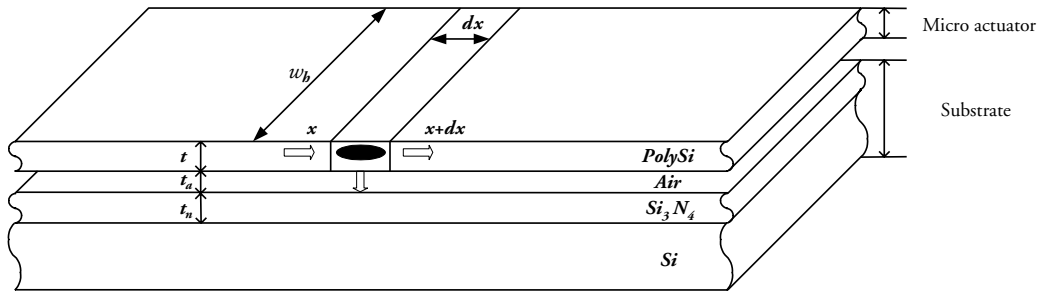
A two-hot-arm thermal actuator (figure 1(*b*)) is operated by using the same strategy of the traditional horizontal thermal actuator. However, in this actuator, the electric current only passes through the outer and inner hot arms. This releases the requirement for the cold arm and flexure to be a part of the electric circuit. It dramatically increases the efficiency of power consumption since all the power consumed in the new thermal actuator contributes to the deflection of the actuator. The flexure can also be thinner than the hot arms because no

(*a*) Traditional one-hot-arm thermal actuator

(*b*) Schematic of a two-hot-arm thermal actuator
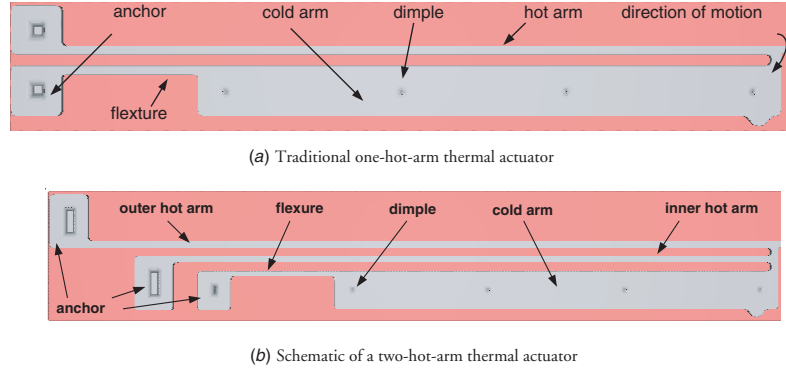
Figure 1. (*a*) Traditional one-hot-arm thermal actuator, (*b*) schematic of a two-hot-arm thermal actuator.

(*a*)

(*b*)
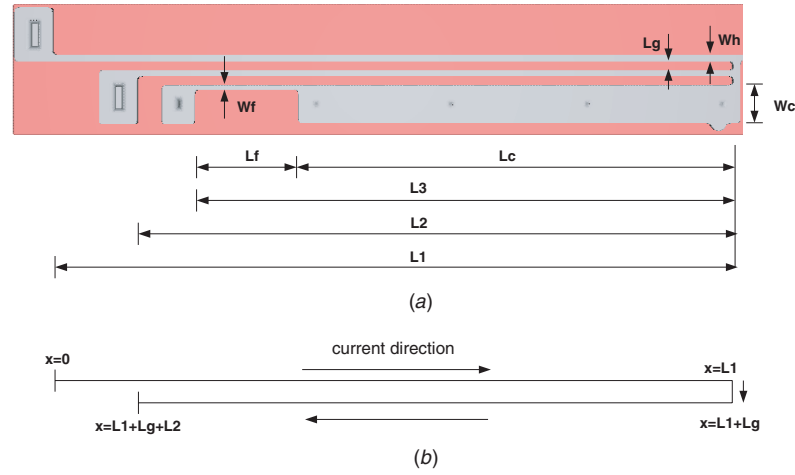
Figure 2. (*a*) Top view of two-hot-arm thermal actuator, (*b*) simplified one-dimensional coordinate system.

Figure 3. Cross section of the actuator for thermal analysis.

current passes through the flexure. This can be used to increase the actuator deflection.

2.1. Electrothermal analysis

The two-hot-arm thermal actuator is usually fabricated by surface micromachining. The size of the cross section of the actuator is much smaller than the actuator length. Therefore, the electrothermal analysis of the two-hot-arm actuator is generally simplified as a one-dimensional problem [14]. The two-hot-arm thermal actuator shown in figure 1(*b*) can be treated as two line-shape microbeams connected in series. Figure 2(*a*) shows the parameters used to describe the geometry of the actuator and figure 2(*b*) shows the coordinate

system for thermal analysis. Since the current only passes through the outer and inner hot arms, the coordinate does not include the cold arm and flexure.

There are three mechanisms of heat flow: conduction, convection and radiation. According to [12, 13], the heat dissipation through radiation to the ambient can be neglected in comparison with the heat losses through conduction to the anchors which are considered as heat sinks, and the heat losses through air to the substrate due to convection.

As shown in figure 3, the heat flow equation is derived by examining a differential element of the microbeam of thickness t, width w_h and length dx [11]. When the heat transfer flow is under steady-state conditions, resistive heating power generated in the element is equal to the heat conduction

313

Figure 4. Boundary conditions of the actuator.

and convection out of the element,

$$-k_p w_h t \left.\frac{dT}{dx}\right|_x + J^2 \rho w_h t \, dx = -k_p w_h t \left.\frac{dT}{dx}\right|_{x+dx}$$
$$+ \frac{S w_h (T - T_s) \, dx}{R_T} \tag{1}$$

where T and T_s are the beam and substrate's temperatures, respectively; k_p is the thermal conductivity of polysilicon, J is the current density, ρ is the resistivity of polysilicon, and S is the shape factor which accounts for the impact of the shape of the element on heat conduction to the substrate [14]. This geometric factor represents the ratio of heat loss from the sides and bottom of the beam to the heat loss from the bottom of the beam only. R_T is the thermal resistance between the polysilicon microbeam and the substrate if the microbeam is wide enough [11]. The thermal resistance, R_T, is given by

$$R_T = \frac{t_a}{k_v} + \frac{t_n}{k_n} \tag{2}$$

where t_a and t_n are the thickness of air above the nitride and the thickness of nitride on the substrate, respectively, and k_v and k_n are the thermal conductivity of air and nitride. The shape factor, S, is given by [14]

$$S = \frac{t}{w_h}\left(2\frac{t_a}{t} + 1\right) + 1. \tag{3}$$

Usually, the resistivity ρ is related to the temperature of polysilicon [11]. The resistivity can be assumed here to have a linear dependency on temperature as

$$\rho = \rho_0[1 + \xi(T - T_s)] \tag{4}$$

where ρ_0 is the resistivity of polysilicon at room temperature and ξ is a constant.

The current density is written as

$$J = \frac{V}{\rho L} \tag{5}$$

where V is the voltage applied to the outer and inner hot arms and L is the length of the polysilicon that current passes through. After taking the limit as $dx \to 0$, equation (1) is simplified to

$$\frac{d^2 T}{dx^2} = \frac{S(T - T_s)}{k_p R_T t} - \frac{J^2 \rho}{k_p}. \tag{6}$$

Substituting equations (5) and (4) into equation (6), the final equation for the thermal model is found to be

$$\frac{d^2 T}{dx^2} = \frac{S(T - T_s)}{k_p R_T t} - \frac{V^2}{L^2 \rho_0 k_p [1 + \xi(T - T_s)]}. \tag{7}$$

In the following, we linearize equation (7) and derive its closed form solution. In equation (7), the second item in the

right-hand side is nonlinear. After using the Taylor series expansion to linearize this item, equation (7) becomes

$$\frac{d^2 T}{dx^2} = \frac{S(T - T_s)}{k_p R_T t} - \frac{V^2}{L^2 \rho_0 k_p}[1 - \xi(T - T_s)]$$

or

$$\frac{d^2 T_\theta}{dx^2} = A^2 T_\theta - B \tag{8}$$

where

$$T_\theta = T - T_s \tag{9a}$$

$$B = \frac{V^2}{L^2 \rho_0 k_p} \tag{9b}$$

$$A^2 = \frac{S}{k_p R_T t} + B\xi. \tag{9c}$$

Equation (8) is a linear differential equation where its solution is

$$T_1 = T_s + \frac{B_1}{A_1^2} + C_1 e^{A_1 x} + C_2 e^{-A_1 x} \tag{10a}$$

$$T_2 = T_s + \frac{B_2}{A_2^2} + C_3 e^{A_2 x} + C_4 e^{-A_2 x}. \tag{10b}$$

In equation (10) T_1 and T_2 are the temperature distribution for the outer and inner hot arms respectively. C_i ($i = 1$ to 4) are some constants to be obtained based upon the boundary conditions applied to the microbeam. Also B_1 and A_1, and B_2 and A_2 are the same as B and A in equation (8), respectively, except that L is replaced by L_1 and L_2, V is replaced by V_1 and V_2, and w is replaced by w_h. V_1 and V_2 are the voltages across the outer and inner hot arms, respectively, which are

$$V_1 = \frac{V}{L_1 + L_2} L_1 \tag{11a}$$

$$V_2 = \frac{V}{L_1 + L_2} L_2. \tag{11b}$$

It should be noted that since L_g in figure 2 is much smaller than L_1 and L_2, it can be assumed to be zero or included in the length of outer hot arm L_1. To obtain C_i we consider figure 4 that shows the boundary conditions. The rate of heat conduction at the connection point of the outer and inner hot arms is shown by q_i. The temperature of the joint point between the outer and inner hot arms is indicated by T_m as seen in figure 4. The anchor pads are assumed to have the same temperature (T_s) of the substrate. According to the continuity of the temperature and rate of heat conduction, five algebraic equations can be written to obtain the unknowns C_i ($i = 1$ to 4) and T_m. These equations using figure 4 and equations (10) in matrix form are
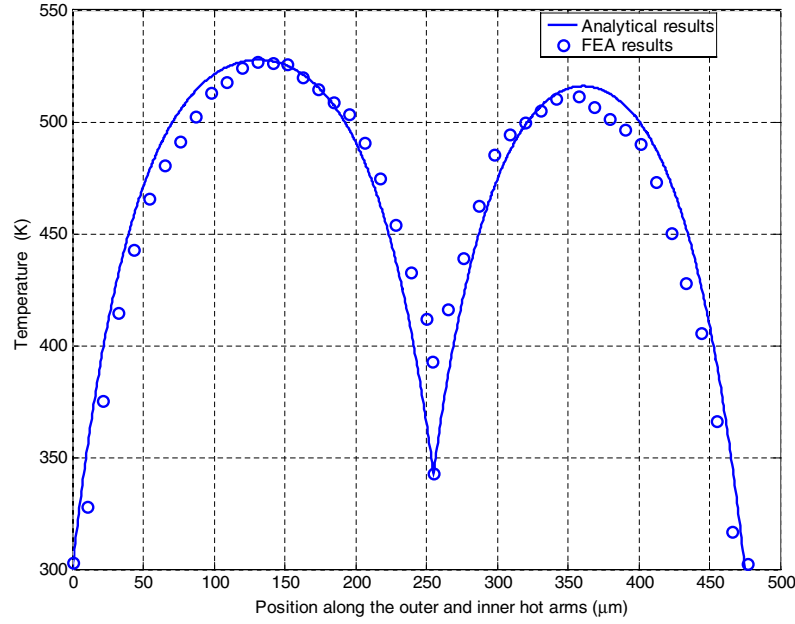
$$\overline{A} X = \overline{B} \tag{12}$$

Figure 5. Temperature distribution along the outer and inner hot arms.

where

$$\overline{A} = \begin{bmatrix} 1 & 1 & 0 & 0 & 0 \\ 0 & 0 & 1 & 1 & 0 \\ e^{A_1(L_1+L_g)} & e^{-A_1(L_1+L_g)} & 0 & 0 & -1 \\ 0 & 0 & e^{A_2 L_2} & e^{-A_2 L_2} & -1 \\ A_1 e^{A_1(L_1+L_g)} & -A_1 e^{-A_1(L_1+L_g)} & A_2 e^{A_2 L_2} & -A_2 e^{A_2 L_2} & -\frac{1}{K_p w_h t R_{\text{cold}}} \end{bmatrix}$$

$$\overline{B} = \begin{bmatrix} -\frac{B_1}{A_1^2} \\ -\frac{B_2}{A_2^2} \\ -T_s - \frac{B_1}{A_1^2} \\ -T_s - \frac{B_2}{A_2^2} \\ -T_s \frac{1}{K_p w_h t R_{\text{cold}}} \end{bmatrix} \qquad X = \begin{bmatrix} c_1 \\ c_2 \\ c_3 \\ c_4 \\ T_m \end{bmatrix}$$

and R_{cold} is the thermal resistance of the cold arm of the thermal actuator.

The heat transfer to the cold arm q_3 in figure 4 is approximated using the approach suggested in [15]. In this approach, by assuming $w_c \gg w_h$, the cold arm is replaced by a quarter circle with radius w_c centered at the actuator's tip. This simplification results in

$$R_{\text{cold}} = \frac{\ln \frac{w_h}{w_c}}{2 k_p t \pi} \tag{13}$$

for the cold arm thermal resistance. Equations (10) along with equation (12) are the closed form solution of the temperature distribution of the two-hot-arm thermal actuator.

To simulate the temperature distribution of the two-hot-arm thermal actuator, the parameters reported in [11, 16] and listed in tables 1 and 2 are used.

Figure 5 shows the temperature distribution along the outer and inner hot arms for the input voltage of 5 V. In the figure, the maximum temperature is shown in the middle of the outer hot arm. In the middle of the inner hot arm, the temperature is slightly lower than the maximum temperature because the length of the outer hot arm is longer than that

Table 1. Material properties.

Material properties	Value	Unit
Young's modulus E	162×10^9	Pa
Poisson's ratio v	0.22	
Thermal expansion coefficient K	3.5×10^{-6}	C^{-1}
Thermal conductivity of polysilicon k_p	41×10^{-6}	W μm^{-1} C^{-1}
Thermal conductivity of air k_v	0.026×10^{-6}	W μm^{-1} C^{-1}
Thermal conductivity of nitride k_n	2.25×10^{-6}	W μm^{-1} C^{-1}
Resistivity of polysilicon ρ_0	20	Ω μm

Table 2. Geometrical data of the two-hot-arm thermal acutator.

Geometrical data	Value	Unit
Length of the outer hot arm L_1	252	μm
Length of the inner hot arm L_2	220	μm
Length of the cold arm L_c	162	μm
Length of the flexure L_f	38	μm
Length of the gap L_g	2	μm
Thickness of polysilicon t_{si}	2	μm
Thickness of air t_a	2	μm
Thickness of nitride t_n	0.6	μm
Width of hot arm w_h	2	μm
Width of flexure w_f	2	μm
Width of cold arm w_c	14	μm

of the inner hot arm. Since the outer and inner hot arms are both connected to the anchor, the temperature at those points is equal to the substrate temperature T_s. At the joint point between the outer and inner hot arms, the temperature changes abruptly. It happens because the cold arm is also connected at that point, which acts as a heat sink.

To evaluate the lumped modeling results, the temperature distribution of the actuator has been simulated by Coventorware® MemETherm solver. This solver can compute the thermal field and the electrical potential resulting from an
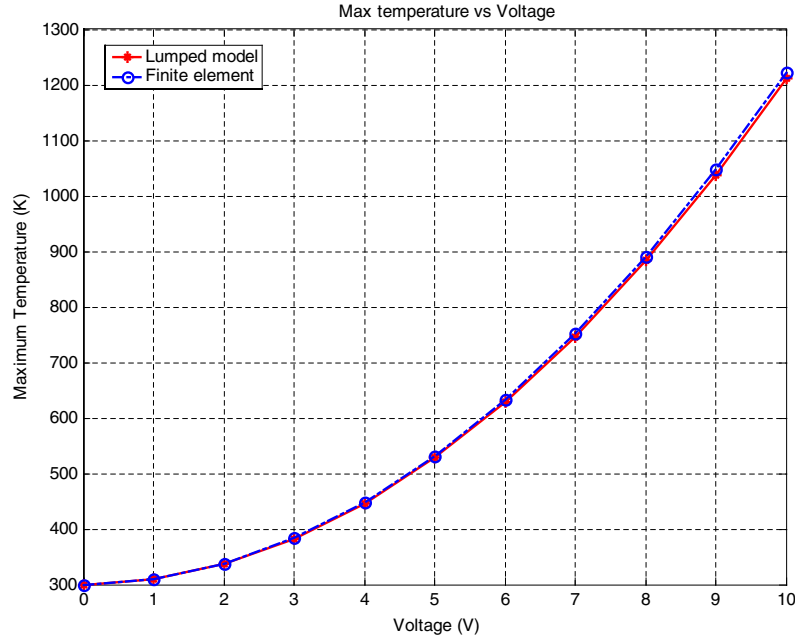
315

Figure 6. Comparison of the maximum temperature as a function of the input voltage.

imposed voltage or current flow through a resistive material. In this simulation, three different physical domain boundary conditions—electrical, thermal and mechanical—are applied. For the electrical boundary condition, a voltage is applied across the outer and inner hot arms. For the thermal boundary conditions, all of the three anchors are set to the substrate temperature. For the mechanical boundary conditions, the three anchors are fixed in all directions to the substrate. The maximum temperature as a function of the input voltage is shown in figure 6. It clearly shows that the maximum temperature increases with the input voltage and the lumped and finite element results are almost identical.

2.2. Thermal-mechanical analysis

Based on the operating principle of the two-hot-arm thermal actuator, it is essential to know the linear thermal expansion of the outer and inner hot arms in order to find the mechanical deflection of the actuator. The temperature distribution of the arms has been defined in equations (10). Using the temperature distribution of the arms, the thermal expansion of the outer and inner hot arms ΔL_1 and ΔL_2 can be given by

$$
\Delta L_1 = K \int_0^{L_1} (T_1 - T_s)\, \mathrm{d}x
$$
$$
= \alpha \left(\frac{B_1}{A_1^2} L_1 + \frac{C_1}{A_1} \mathrm{e}^{A_1 L_1} - \frac{C_1}{A_1} - \frac{C_2}{A_1} \mathrm{e}^{-A_1 L_1} + \frac{C_2}{A_1} \right)
$$

(14)

$$
\Delta L_2 = K \int_0^{L_2} (T_2 - T_s)\, \mathrm{d}x
$$
$$
= \alpha \left(\frac{B_2}{A_2^2} L_2 + \frac{C_3}{A_2} \mathrm{e}^{A_2 L_2} - \frac{C_3}{A_2} - \frac{C_4}{A_2} \mathrm{e}^{-A_2 L_2} + \frac{C_4}{A_2} \right).
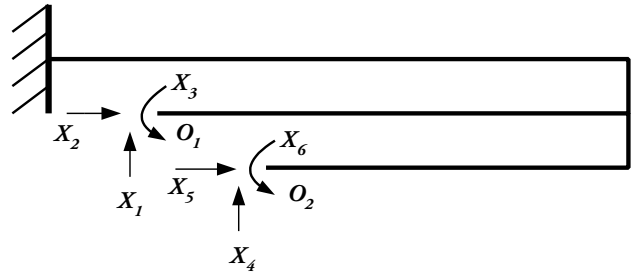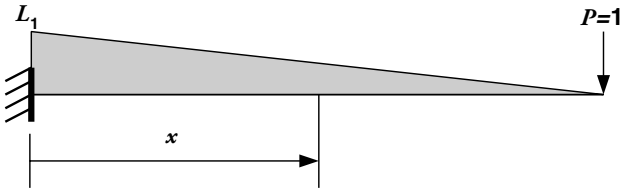$$

(15)

Figure 7. Plane-frame structure of the thermal actuator with six redundants.

where K is the thermal expansion coefficient of the polysilicon.

The structure of the two-hot-arm thermal actuator shown in figure 1 is a plane-frame structure with three fixed bases. Deflection analysis of such structures has been well documented in [17] using force method. This method is applied here to the deflection analysis of the actuator due to the thermal expansion. The actuator is a statically indeterminate structure with the degree of the indeterminacy of six. Two of the constraints at O_1 and O_2 are released and replaced by forces and moments as shown in figure 7. In this method, we assume the actuator undergoes thermal expansion when the inner and cold arms are released from the substrate at O_1 and O_2. Since the thermal expansion is in X direction, the connection points of the inner and cold arms will move only in X direction by $\Delta L_1 - \Delta L_2$ and ΔL_1, respectively. To satisfy the boundary conditions, the connection points must be returned to their initial locations and orientations by applying constraint forces X_i. If we assume that the flexibility coefficients of the connection points for the constrain forces

Figure 8. The bending moment of the outer hot arm due to the virtual force P.

are shown by f_{ij}, X_i are calculated from

$$\begin{bmatrix} f_{11} & f_{12} & f_{13} & f_{14} & f_{15} & f_{16} \\ & f_{22} & f_{23} & f_{24} & f_{25} & f_{26} \\ & & f_{33} & f_{34} & f_{35} & f_{36} \\ & & & f_{44} & f_{45} & f_{46} \\ & \text{Sym} & & & f_{55} & f_{56} \\ & & & & & f_{66} \end{bmatrix} \begin{bmatrix} X_1 \\ X_2 \\ X_3 \\ X_4 \\ X_5 \\ X_6 \end{bmatrix} = \begin{bmatrix} 0 \\ \Delta L_1 - \Delta L_2 \\ 0 \\ 0 \\ \Delta L_1 \\ 0 \end{bmatrix} \quad (16)$$

where each item on the right-hand side of equation (16) represents the displacement of force component X_i in its own direction. The flexibility coefficient f_{ij} is defined as the deflection in i direction due to the unit force acted at j direction. Using the Maxwell principle it can be shown that the flexibility matrix is symmetric, i.e. $f_{ij} = f_{ji}$. Since the approach is well documented in different papers including [17], we only present the final results given in the appendix for the flexibility matrix.

Once the six redundances are obtained, the deflection of the actuator tip can be calculated by the virtual work method [17]. A virtual force P is applied to the free end of the actuator normal to the hot arm. The bending moment of the outer hot arm due to the virtual force is shown in figure 8. The bending moment due to the virtual force as a function of the position of the outer hot arm is given by

$$\overline{M} = (L_1 - x)P. \quad (17)$$

The bending moment of the outer hot arm due to the thermal expansion, i.e. the moment of the outer hot arm due to the six redundances shown in figure 7, can be represented as

$$M = \sum_{i=1}^{2} M_i \quad (18)$$

$$M_1 = X_1 x + X_1(L_2 - L_1) - X_2 L_g - X_3 \quad (19)$$

$$M_2 = X_4 x + X_4(L_3 - L_1) - 2X_5 L_g - X_6 \quad (20)$$

where M_1 is the bending moment of the outer hot arm caused by the redundances X_1, X_2 and X_3, and M_2 is the bending moment of the outer hot arm caused by the redundances X_4, X_5 and X_6. M is the total bending moment of the outer hot arm caused by the thermal expansion. According to the method of virtual work [17], the deflection in the free end of the actuator can be written as

$$u = \int_{L_1} \frac{\overline{M} M}{E I_h} \, \mathrm{d}x = \frac{1}{E I_h} \left(-\frac{\beta_a L_1^3}{3} + \frac{L_1 \beta_a - \beta_b}{2} L_1^2 + L_1^2 \beta_b \right) \quad (21)$$

where β_a and β_b are

$$\beta_a = X_1 + X_4 \quad (22)$$

$$\beta_b = X_1(L_2 - L_1) - X_2 L_g - X_3 \\ + X_4(L_3 - L_1) - 2X_5 L_g - X_6. \quad (23)$$

To evaluate the accuracy of the linear modeling of the actuator deflection, we simulate the two-hot-arm thermal actuator by Coventorware® with MemEThem solver. The lumped and finite element solutions of the beam's tip deflection as a function of the input voltage are shown in figure 9. As seen
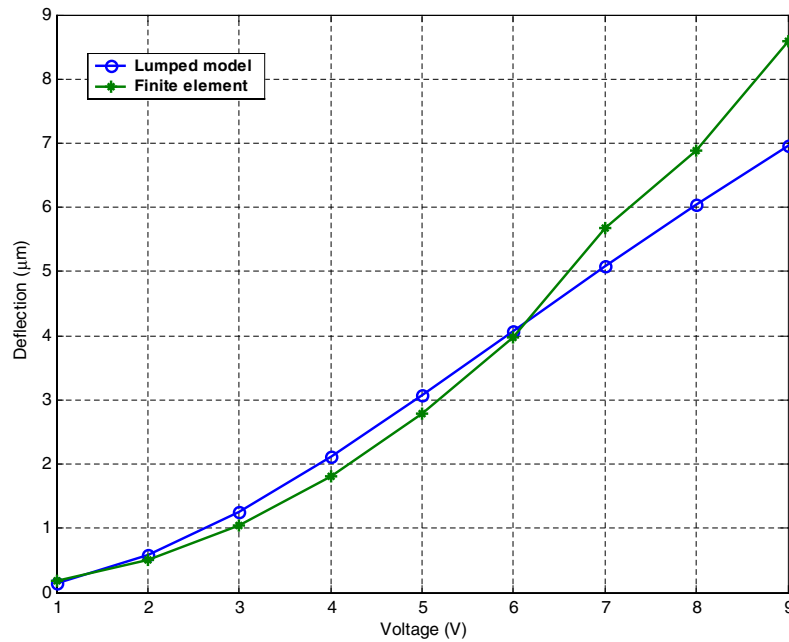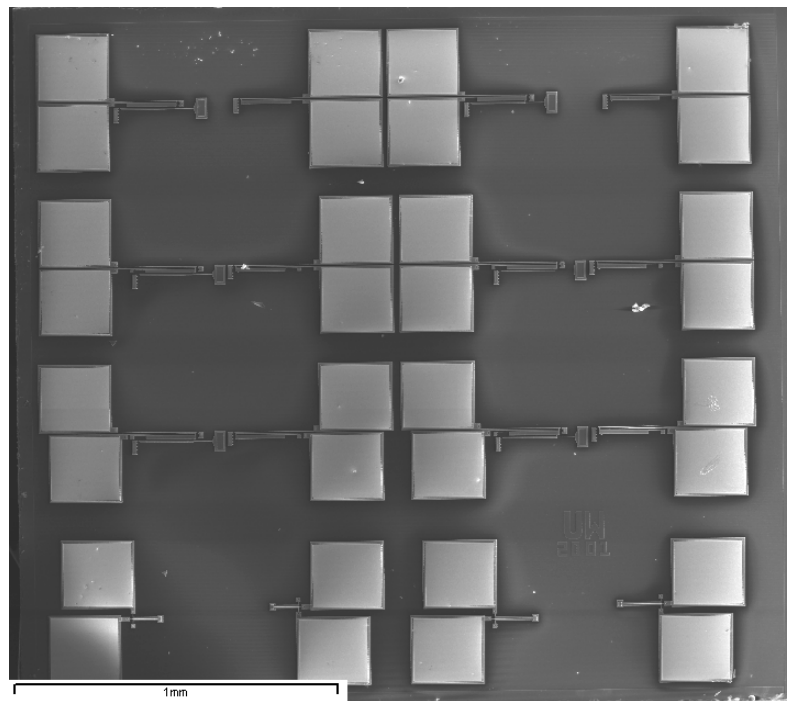

Figure 9. Actuator's tip deflection as a function of the input voltage.
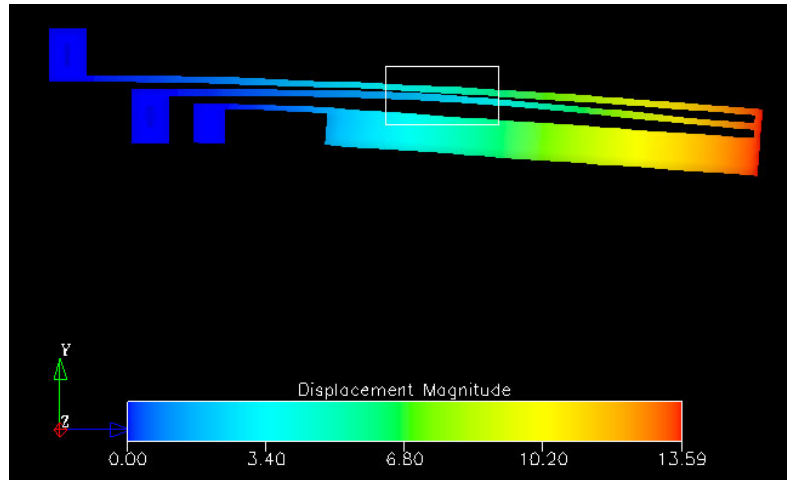
Figure 10. Finit element results of the actuator's deflection at 10 V.

Figure 11. Deflection meter for the two-hot-arm thermal actuator.

Figure 12. The overview of the whole chip after HF release.

in the figure, the lumped model has predicted the beam's deflection very close to the finite element analysis. At higher voltages (temperature) however, the finite element results cross the lumped model curve. This is due to the linear approximation performed in equation (7) and possibly the effect of heat radiation.

In general, the actuators are not operated at high voltages since the inner and outer hot arms may touch each other [9] due to large deflection as seen in figure 10. In this figure, a 10 V is applied to the actuator which has resulted in more than 10 μm deflection. It caused the contact of the inner and outer hot arms as shown in the box in figure 10.
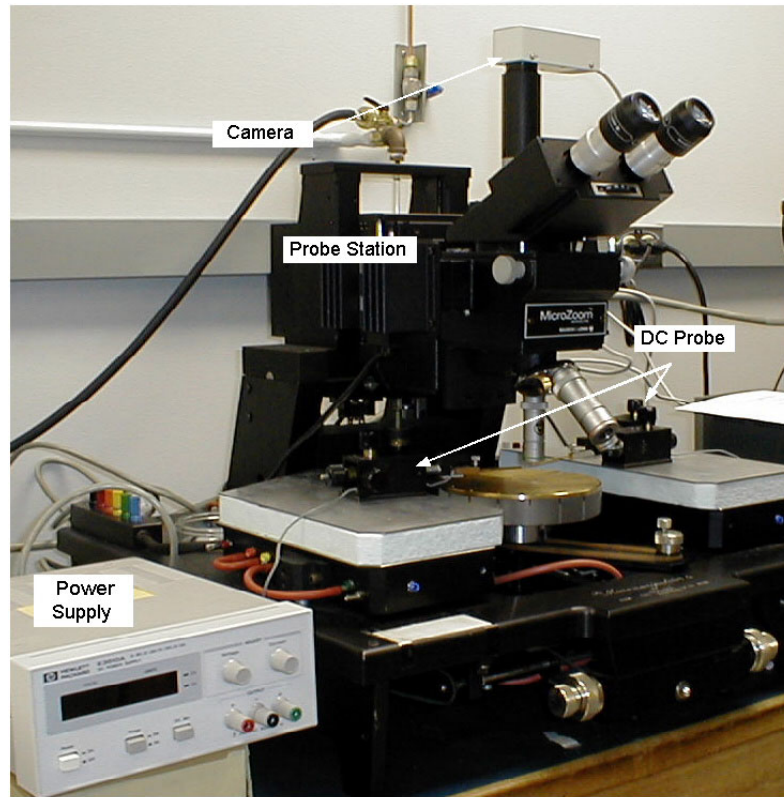
318

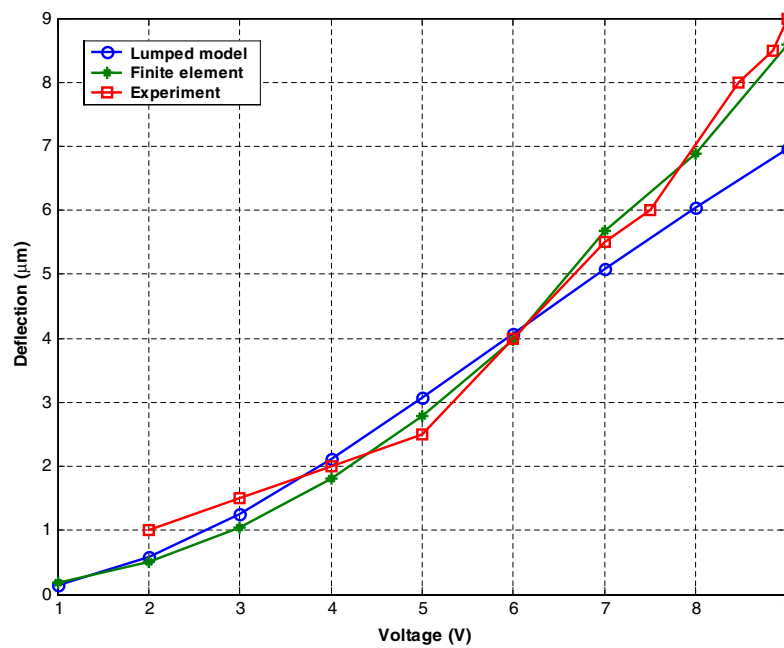**Figure 13.** Experiment equipment for measuring deflection.

**Figure 14.** Comparison of experimental, FE and lumped model deflection results.

3. Fabrication and experiments

The two-hot-arm thermal actuator presented here was fabricated using the 44th production run of the Multi-User MEMS Processes (MUMPs). The whole thermal actuator was constructed out of poly1. In order to reduce the friction effect, dimples were used on the cold arm to reduce the amount of polysilicon in direct contact with the silicon nitride layer. One deflection meter was also considered for easier measurement of the displacement (figure 11). The actuator was released

319

Figure 15. Touching of the outer and inner hot arms at high actuating voltage.
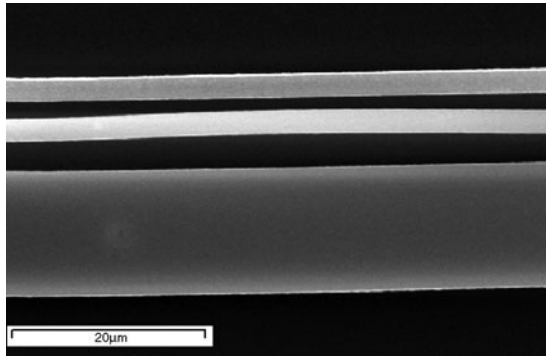

(*a*)
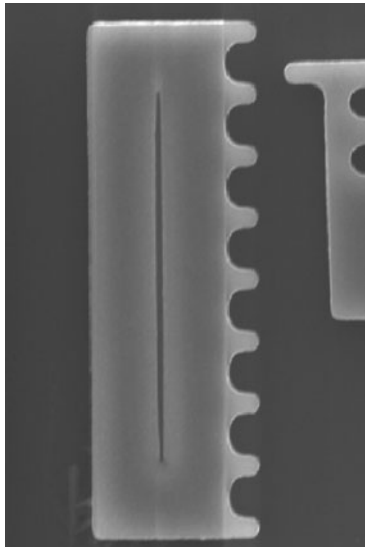
(*b*)

Figure 16. (*a*) Plastic deformation of inner hot arm, (*b*) forward bending of two-hot-arm thermal actuator.

using HF release process at the clean room of the University of Waterloo. Figure 12 shows the scanning electron micrograph (SEM) of the chip.

In the experiments, a power supply with a 15 V (dc) tuning range and two dc probes were employed to apply a voltage to the thermal actuator. In order to capture the deflection, a CCD camera was installed on the top of the probe station. The power supply was tuned from 2 to 11 V and the camera was used to record the actuator deflections. The exact deflection of the thermal actuator at any actuating voltage was then obtained by enlarging the picture at the deflection zone. Figure 13 shows the experimental setup. The results of the experiments are plotted in
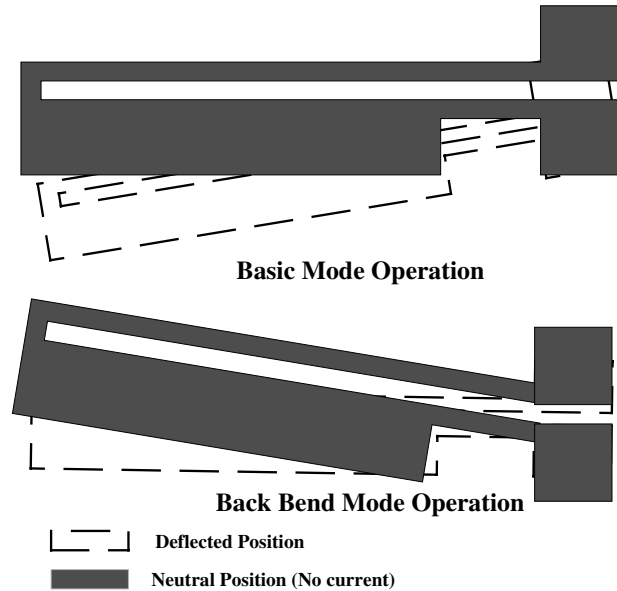
**Figure 17.** Two modes of the traditional thermal actuator operation.

figure 14. To evaluate the lumped model, the deflection of the actuator's tip at different voltages obtained from the lumped and finite element models is shown with the experimental results.

4. Discussion

In figure 10, the simulation results show that the outer and inner hot arms could touch each other at a high actuating voltage. This phenomenon occurred during the experiments. Figure 15 shows the touching of the outer and inner hot arms when the actuator was subjected to 9.0 V. It was also observed that after the two arms contacted each other, the thermal actuator did not return completely to its original place upon removing the voltage. After zooming at the middle of the two hot arms, a curve was found in the inner hot arm (figure 16(*a*)), which showed that the thermal actuator had undergone a plastic deformation. As a result, the inner hot arm becomes shorter and causes a permanent deflection as seen in figure 16(*b*).

A traditional thermal actuator can operate in two modes [18]. Figure 17 shows both modes of operation for the actuator.

In the basic mode, the thermal actuator is operated as described before. The back-bent mode occurs after the driving current is increased above the level required for the maximum deflection which results in reshaping the hot arm. After reshaping, the hot arm is shorter than its original length and therefore the thermal actuator moves to a negative position. A back-bent thermal actuator still can be used as a traditional thermal actuator except that the zero-deflection position is shifted. For the two-hot-arm thermal actuator, back bending was also found in the experiments, when the voltage reached 11 V and applied for a few seconds. Figure 18 shows the back bending of the two-hot-arm thermal actuator.

(a)   (b)
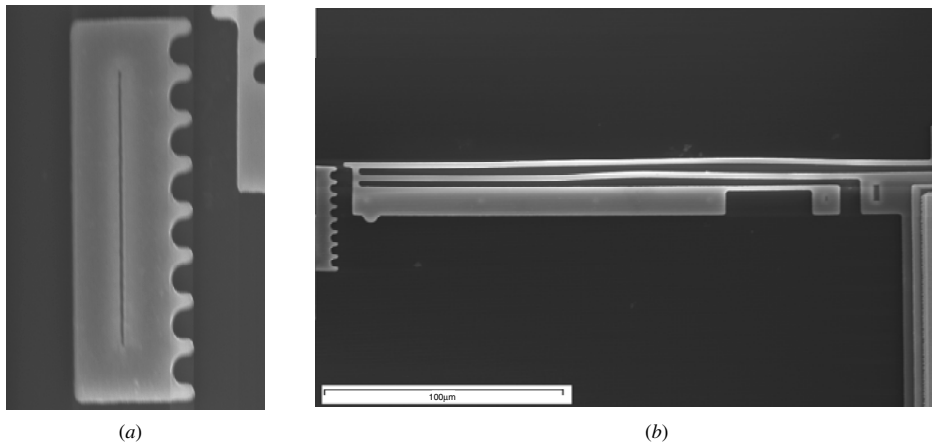
Figure 18. (*a*) Close view of the actuator tip, (*b*) back bending of two-hot-arm thermal actuator.
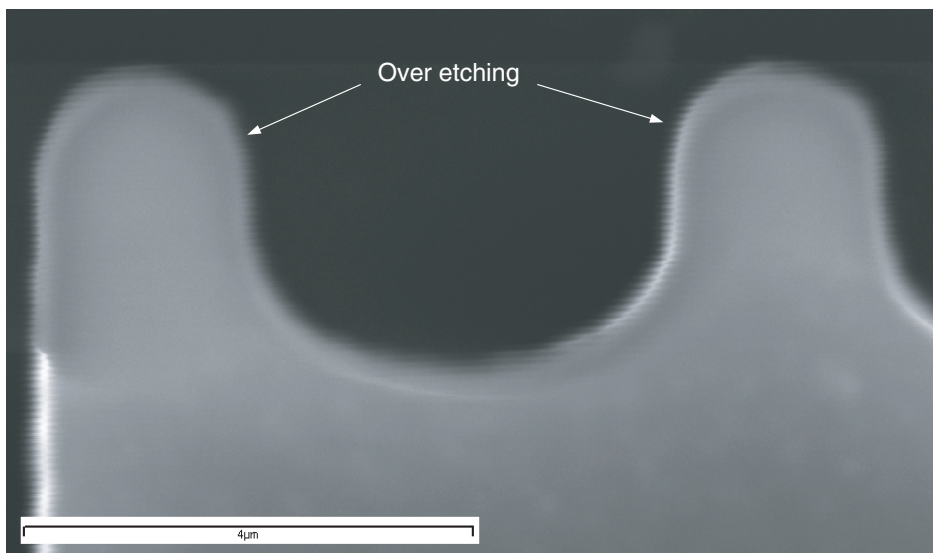
Figure 19. The overetching of the teeth of the deflection meter.

At high actuating voltage, two different phenomena are found: the touching of the two hot arms and back bending. Both of them are not desirable for most thermal actuator applications. Accurate models can be used to predict both magnitude and duration of safe working voltages. Fabrication tolerance should also be concerned. For example, the etching time in HF etchant, the mask resolution and the photolithography quality can affect the final geometry of the actuator significantly. Figure 19 shows the result of these effects and as it can be seen, the teeth of the deflection meter have become circular instead of rectangular.

5. Conclusions

A lumped model for the two-hot-arm thermal actuator was proposed. In the electrothermal analysis, heat conduction to the substrate through the air and nitride which is the most important heat transfer mechanism was considered. To obtain a closed form solution, the nonlinear part was linearized by using Taylor series expansion. Finite element results were in good agreement with lumped model in a large temperature range. The thermal-mechanical analysis was proceeded by using virtual work theory. The two-hot-arm thermal actuator was fabricated and tested. Experimental results were also in good agreement with lumped model, which proved the accuracy of the modeling approach. The model can effectively be used for design and optimization of two-hot-arm horizontal thermal actuators and also for prediction of their dynamic response.

Appendix

$$f_{11} = \frac{1}{EI_h}\left(\frac{L_2^3}{3} + L_2^2 L_g + \frac{L_1^3}{3} + L_2^2 L_1 - L_1^2 L_2\right)$$

$$f_{21} = -\frac{1}{2EI_h}\left(2L_1 L_2 L_g + L_2 L_g^2 - L_1^2 L_g\right)$$

$$f_{31} = -\frac{1}{2EI_h}\left(L_1 L_2 + L_2 L_g + L_2^2 - L_1^2\right)$$

$$f_{41} = \frac{1}{2EI_h}\left(2L_1^3 - L_1^2 L_2 + 2L_2 L_g L_3 + 2L_2 L_1 L_3 - L_1^2 L_3\right)$$

$$f_{51} = \frac{1}{2EI_h}\left(2L_1^2 L_g - 4L_1 L_2 L_g - 3L_g^2 L_2\right)$$

$$f_{61} = -\frac{1}{2EI_h}\left(2L_1 L_2 + 2L_2 L_g - L_1^2\right)$$

$$f_{22} = \frac{1}{3EI_h}\left(3L_1 L_g^2 + L_g^3\right)$$

$$f_{32} = \frac{1}{2EI_h}\left(2L_1 L_g + L_g^2\right)$$

$$f_{42} = \frac{1}{2EI_h}\left(2L_3 L_1 L_g - L_g^2 L_2 - L_1^2 L_g\right)$$

$$f_{52} = \frac{2L_1 L_g^2}{EI_h}$$

$$f_{62} = \frac{1}{2EI_h}\left(2L_1 L_g + L_g^2\right)$$

$$f_{33} = \frac{1}{EI_h}(L_1 + L_2 + L_g)$$

$$f_{43} = \frac{1}{2EI_h}\left(L_1^2 - L_1 L_3 - L_3 L_g\right)$$

$$f_{53} = \frac{1}{2EI_h}\left(3L_g^2 + 4L_1 L_g\right)$$

$$f_{63} = \frac{1}{EI_h}(L_1 + L_g)$$

$$f_{44} = \frac{L_f^3}{3EI_f} + \frac{L_c(L_3 + L_f)\left(2L_c^3 + 6L_c L_f L_3\right)}{2EI_c\left(3L_c^2 + 6L_c L_f\right)}$$
$$+ \frac{1}{3EI_h}\left(6L_3^2 L_g + L_1^3 + 3L_1 L_3^2 - 3L_3 L_1^2\right)$$

$$f_{54} = -\frac{1}{EI_h}\left(2L_1 L_g L_3 + 2L_g^2 L_3 - L_1^2 L_g\right)$$

$$f_{64} = -\frac{L_f^2}{2EI_f} - \frac{L_c(L_3 + L_f)}{2EI_c}$$
$$- \frac{1}{2EI_h}\left(4L_3 L_g - L_1^2 + 2L_1 L_3\right)$$

$$f_{55} = \frac{4L_g^2 L_1}{EI_h} + \frac{8L_g^3}{3EI_h}$$

$$f_{65} = \frac{1}{EI_h}\left(2L_g L_1 + 2L_g^2\right)$$

$$f_{66} = \frac{1}{EI_h}(L_1 + 2L_g) + \frac{L_f}{EI_f} + \frac{L_c}{EI_c}.$$

In the above equations, E is the Young's modulus of polysilicon, I_h, I_c and I_f are the moment of inertia for the hot, and cold arms and the flexure, respectively.

References

[1] Shimoyana I, Yasuda T and Miura H 1997 Cmos drivable electrostatic microactuator with large deflection *Micro ELectro Mechanical System, MEMS'97 10th Annual International Workshop* (Piscataway, NJ: IEEE) pp 90–5

[2] Nguyen T C H, Tang W C and Howe R T 1989 Laterally driven polysilicon resonant microstructures *Sensors Actuators* A **20** 25–32

[3] Ahn C H and Allen M G 1993 A fully integrated surface micromachined magnetic microactuator with a multilevel meander magnetic core *J. Microelectromech. Syst.* **2** 15–22

[4] Brand O, Lagorce L K and Allen M G 1999 Magnetic microactuators based on polymer magnets *J. Microelectromech. Syst.* **8** 2–9

[5] Christenson T, Shrobis K, Landon M, Guckel H, Klein J and Lovell E G 1992 Thermo-magnetic metal flexure actuators *Technical Digest of IEEE Solid State Sensor and Actuator Workshop* (Piscataway, NJ: IEEE) pp 73–5

[6] Comtois J H and Bright V M 1997 Applications for surface-micromachined polysilicon thermal actuators and arrays *Sensors Actuators* A **58** 19–25

[7] Cowan W D and Bright V M 1997 Vertical thermal acutators for micro-opto-electro-mechanical systems *Proc. SPIE* **3226** 137–46

[8] Rbrish P R, Field L A, Burresci D L and Rubby R C 1996 Micromachined 1 × 2 optical fiber switch *Sensors Actuators* A **52-54** 311–5

[9] Burns D M and Bright V M 1997 Design and performance of a double hot arm polysilicon thermal actuator *Proc. SPIE* **3224** 296–306

[10] Bright V M, Comtois J H and Phipps M W 1995 Thermal microactuators for surface micromachining processes *Proc. SPIE* **2642** 10–21

[11] Huang Q-A and Lee N K-S 1999 Analysis and design of polysilicon thermal flexure actuator *J. Micromech. Microeng.* **9** 64–70

[12] Huang Q-A and Lee N K-S 1999 Analytical modeling and optimazation for a laterally-driven polysilicon *Microsyst. Tech.* **5** 133–7

[13] Lerch Ph, Kara-Slimane C, Romanowicz B and Renaud Ph 1996 Modelization and characterization of asymmetrical thermal micro-actuators *J. Micromech. Microeng.* **6** 134–7

[14] Lin L and Chiao M 1996 Electrothermal response of lineshape microstructures *Sensors Actuators* A **55** 35–41

[15] Bayazitoglu Y and Necati Ozisik M 1988 *Elements of Heat Transfer* (New York: McGraw-Hill)

[16] Shishkoff A, Koester D, Mahedevan R and Marcus K 2001 *Multi-User MEMS Process (MUMPs) Introduction and Design Rules* 6th edn, Cronos Integrated Microsystems, A JDS Uniphase Company, 3026 Cornwallis Road, Research Triangle Park, NC 27709

[17] Elms D G 1970 *Linear Elastic Analysis* (London: BT Batsford)

[18] Bright V M, Reid J R and Butler J T 1998 Automated assembly of flip-up micromirrors *Sensors Actuators* A **66** 292–8